ACS APPLIED NANO MATERIALS

www.acsanm.org Article

Se-Doped Magnetic Co–Ni Spinel Ferrite Nanoparticles as Electrochemical Catalysts for Hydrogen Evolution

Mohamed Jaffer Sadiq Mohamed, Serkan Caliskan, Mohammed Ashraf Gondal,* Munirah Abdullah Almessiere, Abdulhadi Baykal, Yassine Slimani, Khaled Abdelsabour Elsayed, Muhammad Hassan, Ismail Abdullah Auwal, Abdul Zeeshan Khan, Asif Ali Tahir, and Anurag Roy*

Cite This: https://doi.org/10.1021/acsanm.3c00464 Read Online

ACCESS | Metrics & More | Article Recommendations | Supporting Information

ABSTRACT: The magnetic $Co_{0.5}Ni_{0.5}Fe_2O_4$ spinel ferrites (NSFs) with various (x%) Se (x = 0.00–0.20) were synthesized via the sol–gel combustion route in conjunction with an advanced green laser ablation method. The structure and morphology of NSFs were explored through various physicochemical techniques. Interestingly, Se doping has a crucial impact on NSFs' magnetic properties. While, at room temperature, the pristine sample exhibits a superparamagnetic-like behavior, the pristine sample and all doped CoNi NSFs + x% Se (x = 0.05–0.20) samples exhibited a high value of coercivity and remanence at 10 K, indicating their hard magnetic properties. Our findings indicate that Se can be harnessed to tune the magnetic properties of $CoNiFe_2O_4$ structures. In addition, improving effective electrocatalysts for hydrogen evolution reaction (HER) efficiency through water splitting is also vital to overcoming the impending energy crisis due to the rapid depletion of fossil fuels and their injurious impact on the environment. Hence, the optimized ideal catalysts CoNi NSFs + x% Se (x = 0.15) were developed, which outperformed as electrocatalysts for HER with a Tafel slope of 91 mV/dec and a very low overpotential of 173.5 mV at a current density of 10 mA/cm^2, which could be attributed to a large number of electrochemically active surface area (5.2 cm^2), accelerated electron mobility at the electrocatalysts/electrolyte interface, and long-term stability.

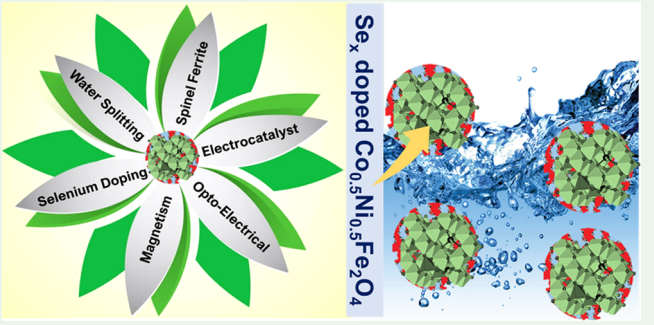

KEYWORDS: *ferrite, hydrogen, laser ablation, magnetic, water splitting*

INTRODUCTION

The high fossil fuel consumption is threatening the environment and also causing rapid depletion of nonrenewable energy resources.[1,2] This situation can be tackled by upgrading sustainable energy and storage technologies that are cheap, renewable, and eco-friendly.[3] Hydrogen fuel is considered a promising clean energy resource to compensate for the growing energy demand and to mitigate the climate change effects, etc.[4] Electrocatalytic water splitting is a viable green energy technology for large-scale hydrogen production. Most of the research work in catalytic water splitting is concentrated on preparing effective and long-lasting catalytic material to boost the hydrogen evolution reaction (HER).[5,6]

Recent technological developments have led to the need for more sophisticated functionalized nanoparticles that can be used in various applications.[7] Spinel ferrite magnetic nanoparticles are absorbed because of their tunable optical, magnetic, and electrochemical properties.[8,9] The doping of external elements into spinel ferrites can substantially enhance the effectiveness of these nanoparticles in the respective field.

Cobalt ferrite ($CoFe_2O_4$) is a spinel ferrite with high mechanical hardness, reasonable magnetic anisotropy, and good chemical stability.[10] As a result of its unique functional properties, $CoFe_2O_4$ has been studied extensively during the last decade. On the other hand, nickel ferrite ($NiFe_2O_4$) exhibits an inverse spinal structure and has been used in many applications, including transformer cores, microwave devices, media recording, energy storage, and HER.[11] The relatively smaller size of a nickel (II) ion, compared with cobalt (II), also causes it to have a smaller coercivity as well as lower magnetocrystalline anisotropy than that of cobalt (II).[12] So, the inclusion of both ions into the spinal ferrite structure would be an exciting strategy to develop spinel ferrites' magnetic and electrochemical properties.

In addition, further alterations in the spinal ferrite structure are carried out by doping with external impurity elements to

Received: February 1, 2023
Accepted: April 14, 2023

Scheme 1. Schematic Representation of Se-Doped CoNi NSFs via Laser Ablation Showing Improvement in Electrochemical Active Surface Area (ECSA)

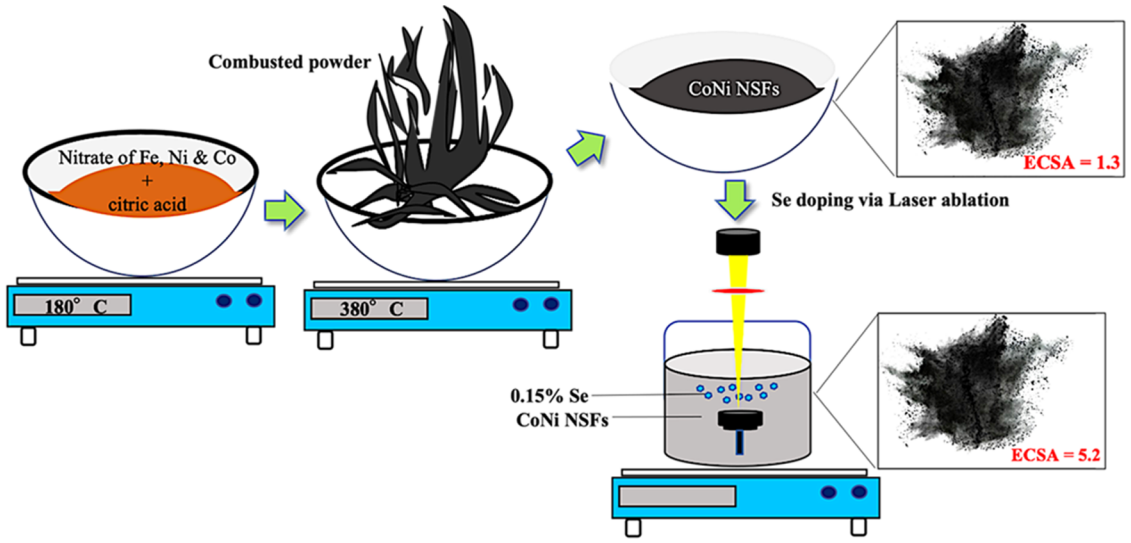

study their response toward magnetic and electrochemical properties. Chen et al. stated the preparation of Co−Ni NSFs, which were derived from the metal-organic framework (MOF) calcination and utilized as a catalyst for oxygen evolution reaction (OER).[13] Such a rational catalyst design provided exceptional OER performance by demonstrating 50 mA/cm^2 at a low overpotential of 265 mV. Abbas et al. worked on synthesizing Al^{3+}-doped $CoFe_2O_4$ NPs using the sol−gel method.[14] The photodegradation efficiency of Al^{3+}-doped cobalt ferrite was recorded to be 83% for a 120 min light illumination, which was much better than that of an undoped sample (58%). Umar et al. studied the fabrication of BLFSO (Se and La codoped $BiFeO_3$) nanosheets via sol−gel and coprecipitation routes.[15] A structural transformation was observed in the synthesized BLFSO crystals from perovskite rhombohedral to orthorhombic phase. This phase transformation helped to lower the material's band gap from 2.04 to 1.76 eV by introducing 50% Se doping in the matrix. Slimani *et al.* stated the synthesis of In^{3+}-doped CoNi spinel ferrite using the solution-combustion method.[16] Depending upon the dopant concentration, the In^{3+} ions were predicted to replace the Fe^{3+} ions in the matrix at Td (tetrahedral) and Oh (octahedral) sites.

In this work, a simple sol−gel combustion method was applied to prepare CoNi NSFs followed by Se doping via an advanced green laser ablation route. The synthesized nanoparticles (with and without Se doping) are characterized systematically to investigate the structural, morphological, magnetic, and electrochemical activities for HER features. Also, the present work aims to find a feasible route to develop a transition-metal-oxide-based efficient electrocatalyst as a superior electrode for future hydrogen fuel cell applications. Magnetic metal oxide catalysts open the possibility of catalytic control, employing an external magnetic field to separate the catalyst from the reaction products.

EXPERIMENTAL SECTION

CoNi NSFs + x% Se (x = 0.00−0.20) were prepared using a modified sol−gel autocombustion process followed by a green laser ablation technique (Scheme 1).[17] The detailed synthesis procedure is given in the Supporting Information (S1).

Physical Measurement. The synthesized samples for various physicochemical analyses were described previously,[17] and brief information has been given in the Supporting Information (S2).

Electrochemical Characterization. A computer-controlled potentiostat (Metrohm AutoLab PGSTAT302N) was used to conduct the electrochemical HER performances of CoNi NSFs + x % Se (x = 0.00−0.20) in a standard three-electrode chemical cell. The electrochemical cell contained glassy carbon as the working electrode, Ag/AgCl electrode (3.5 M KCl solution) as the reference electrode, and platinum electrode as the counter electrode submerged in 0.5 M H_2SO_4 as an electrolyte (pH = 0.3). The working electrode was bare and electrocatalyst-modified glassy carbon (GC) electrodes with a 3 mm diameter. The following steps were employed to prepare the ink and electrode fabrication process: 4 mg of catalyst was thawed in 80% water + 20% ethanol (in volume) mixture containing 80 μL of 5% Nafion solution. The ultrasonication was carried out for 30 min to ensure that the solution was completely dispersed. The modified GC electrode was prepared by 10 μL drop cast of the above mixture, and then the electrode was dried at 80 °C for 2 h for a catalyst loading of 0.285 mg/cm^2. The catalytic performance of the electrodes was evaluated by LSV (linear sweep voltammetry) with a 10 mV/s scan rate in a 0.5 M H_2SO_4 aqueous solution. The reversible hydrogen electrode potential (E_{RHE}) was applied to facilitate the comparison of prepared electrodes at all potentials and evaluated by using the Nernst relation ($E_{RHE} = E_{applied} + 0.0591 \cdot pH + E_{Ag/AgCl}$),[1] where $E_{applied}$ and $E_{Ag/AgCl}$ are the applied potential and reference electrode potential, respectively, and equal to 0.198 V vs RHE. The measurements of electrochemical impedance spectroscopy (EIS) were performed from 10^{-1} to 10^5 Hz with a 10 mV amplitude. The electrodes' ECSA (electrochemically active surface area) can be calculated (ECSA = C_{dl}/C_s). The C_{dl} (double-layer capacitance) value of the representative electrodes was evaluated by measuring the cyclic voltammetry (CV) in a nonfaradic region at different scan rates (i.e., 20−120 mV/s). The C_s is the specific capacitance (i.e., 0.040 mF/cm^2).[13]

RESULTS AND DISCUSSION

XRD Analysis. The microstructure CoNi NSFs + x% Se (x = 0.00−0.20) has been screened by X-ray diffraction (XRD) analysis as illustrated in Figure 1, indicating the presence of a pure phase of spinel ferrite of $CoFe_2O_4$ (JCPDS card: 22−1086). Moreover, the purity of the spinel phase was approved via Rietveld refinement fitting that used experimental XRD data employing Match 3! Fullprof software. The crystal size, cell constant, volume, and reliability parameters are presented

https://doi.org/10.1021/acsanm.3c00464
ACS Appl. Nano Mater. XXXX, XXX, XXX−XXX

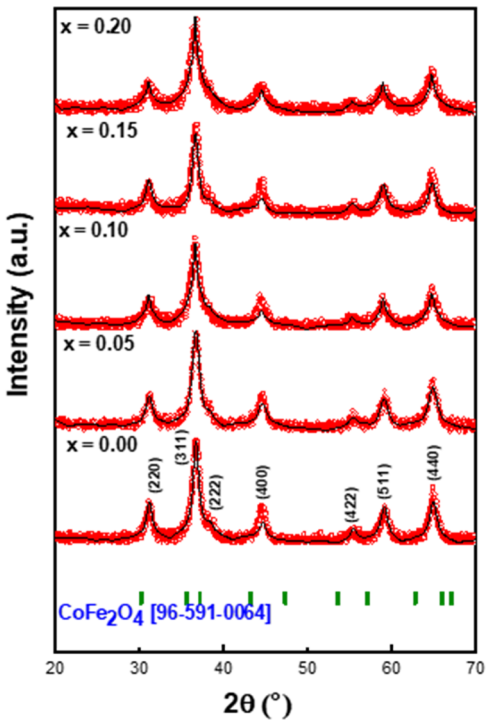

Figure 1. X-ray diffraction powder patterns of CoNi NSFs + x% Se (x = 0.00−0.20).

in Table S1. It was found that the cell constants are increased by increasing the amount of Se due to the expansion in the CoNi NSF crystal. The different intensities of (220) and (400) diffraction peaks are slightly changed; when increased, the quantity of Se is a result of the stresses in the crystal in the direction of the (220) and (400) planes.[18] The Debye−Scherrer equation based on the (311) peak was used to calculate the average crystal sizes and found within a 13−24 nm range. The lattice strain of CoNi NSFs + x% Se (x = 0.00−0.20) was estimated via the Williamson−Hall (W−H) equation[19] by plotting the straight line of $\beta\cos\theta$ vs 4 $\sin\theta$ as shown in Figure S1. The slope of the W−H plots indicated the lattice strain of all samples, as given in Table S1. In all, ratios showed a positive strain due to the samples holding a tensile strain by adding Se.

SEM and TEM Analyses. The microstructure of CoNi NSFs + x% Se (x = 0.00−0.20) was analyzed through scanning electron microscope (SEM), as revealed in Figure S2a−e. The ratios show an aggregation of tiny spherical particles. The CoNi NSFs + x% Se (x = 0.00−0.20) revealed a high porosity in bare CoNi NSFs (x = 0.0) and decreased after increasing the Se content in the matrix. The composition of CoNi NSFs + x% Se (x = 0.00−0.20) was recorded by EDX and is presented in Figure 2a. The energy-dispersive X-ray spectroscopy (EDX) revealed the occurrence of the Ni, Fe, Co, O, and Se elements, which indicates the efficacy of the green laser ablation method. For further morphological analysis of CoNi NSFs + x% Se (x = 0.20), transmission electron microscope (TEM) and high-resolution TEM (HR-TEM) were employed, and such images are presented in Figure 2b−e. The TEM image demonstrated the semicubic particles with different sizes. The HR-TEM image confirmed the structure of pure CoNi NSFs by calculating the lattice planer using GATAN software, which revealed that 0.17 and 0.11 nm correspond to the Miller indices (422) and (355), respectively.

Surface Area Analysis. The surface area and pore size distribution of CoNi NSFs + x% Se (x = 0.00−0.20) NSFs were analyzed using the nitrogen adsorption−desorption isotherm technique (Figure 3 and Table S2). The Brunauer−Emmet−Teller (BET) isotherm of $CoSeFeO_4$ indicated a type III pattern (H3 hysteresis), reflecting the presence of mesoporous characteristics with the addition of Se. Bhujun et al. have reported a similar mesoporous generation with Al metal doping on spinel ferrite.[20] CoNi NSFs + x% Se (x = 0.00) showed a surface area of 40 m^2/g and a pore volume of 0.29 cm^3/g, which then increased to the maximum of 90 m^2/g and 0.57 cm^3/g with Se addition. The Barrett−Joyner−Halenda (BJH) pore size distribution indicates a concomitant reduction in pore diameter from 18 to 30 nm (x = 0.00−0.20). Overall, the analysis clearly indicates that the surface textural variation with Se addition tends to enhance the surface area and pore volume of CoNi NSFs.

FTIR Analysis. Figure S3 presents the Fourier-transform infrared spectroscopy (FTIR) spectra of CoNi NSFs + x% Se (x = 0.00−0.20) in the range of 400−4000 cm^{-1}. The spectra displayed two typical absorption bands $\nu1$ and $\nu2$ at 404 and 541 cm^{-1}, respectively, which are well-known characteristics of spinel ferrites.[21] The 404 cm^{-1} acts as the metal-oxygen vibrations in the octahedral site, where 541 cm^{-1} represents vibrations of metal-oxygen in the tetrahedral site.[22] These results approved the formation of Co−Ni spinel ferrite.

XPS Analysis. X-ray photoelectron spectroscopy (XPS) study was conducted on CoNi NSFs + x% Se (x = 0.00−0.20). Based on the survey scan conducted across a wide energy range, as seen in Figure 4a, each sample element was successfully identified such as Ni 2p, Fe 2p, Co 2p, O 1s, and Se 3d. The binding energies of the representative elements were all adjusted with the reference C 1s peak (284.8 eV). Figure 4b shows the core level spectrum of Ni $2p_{3/2}$ at a binding energy of 855.3 eV with its overlapped satellite peak at 862.9 eV and Ni $2p_{1/2}$ peak at 872.9 eV with its satellite peak at 879.3 eV.[23] The deconvoluted Ni $2p_{3/2}$ and Ni $2p_{1/2}$ spectra exhibited two characteristic peaks, revealing the presence of Ni^{2+} and Ni^{3+} states.[24] Figure 4c shows the core level spectra of Fe $2p_{3/2}$ at 710.2 eV and Fe $2p_{1/2}$ at 723.5 eV, with ΔE = 13.3 eV proving Fe existence in the +3 oxidation state. Further, the deconvolution of Fe spectra did not introduce any peaks, indicating the presence of Fe^{3+} ions only at the octahedral sites in the ferrite structure. The core spectra for Co $2p_{3/2}$ were detected at 780.4 eV and Co $2p_{1/2}$ at 795.5 eV, along with two corresponding satellite peaks at 785.6 and 803.1 eV, respectively,[25] as shown in Figure 4d. Figure 4e shows the broad peak of the O 1s spectrum that was deconvoluted into three characteristic peaks at 526.8, 530.4, and 533.1 eV. In the case of complex molecules containing transition metals, it is challenging to assign the correct oxidation number of oxygen.[26] According to Duplin's interpretation,[27] the lowest binding energy could be associated with the O^{2-} state, the middle binding energy to the oxygen state, and the higher binding energy to the adsorbed oxygen species. Finally, the Se 3d (Figure 4f) core level spectrum at 55.6 eV was deconvoluted to obtain the spin−orbit coupling between $3d_{5/2}$ and $3d_{3/2}$ at 53.1 and 55.8 eV, respectively.[28]

Magnetic Property Analysis. Magnetic properties of CoNi NSFs + x% Se (x = 0.00−0.20) are elucidated through measurements of magnetization (M) versus an external field (H) in the range of ±70 kOe. Figure 5 illustrates the associated $M(H)$ hysteresis loops at room temperature (RT), for which

https://doi.org/10.1021/acsanm.3c00464
ACS Appl. Nano Mater. XXXX, XXX, XXX−XXX

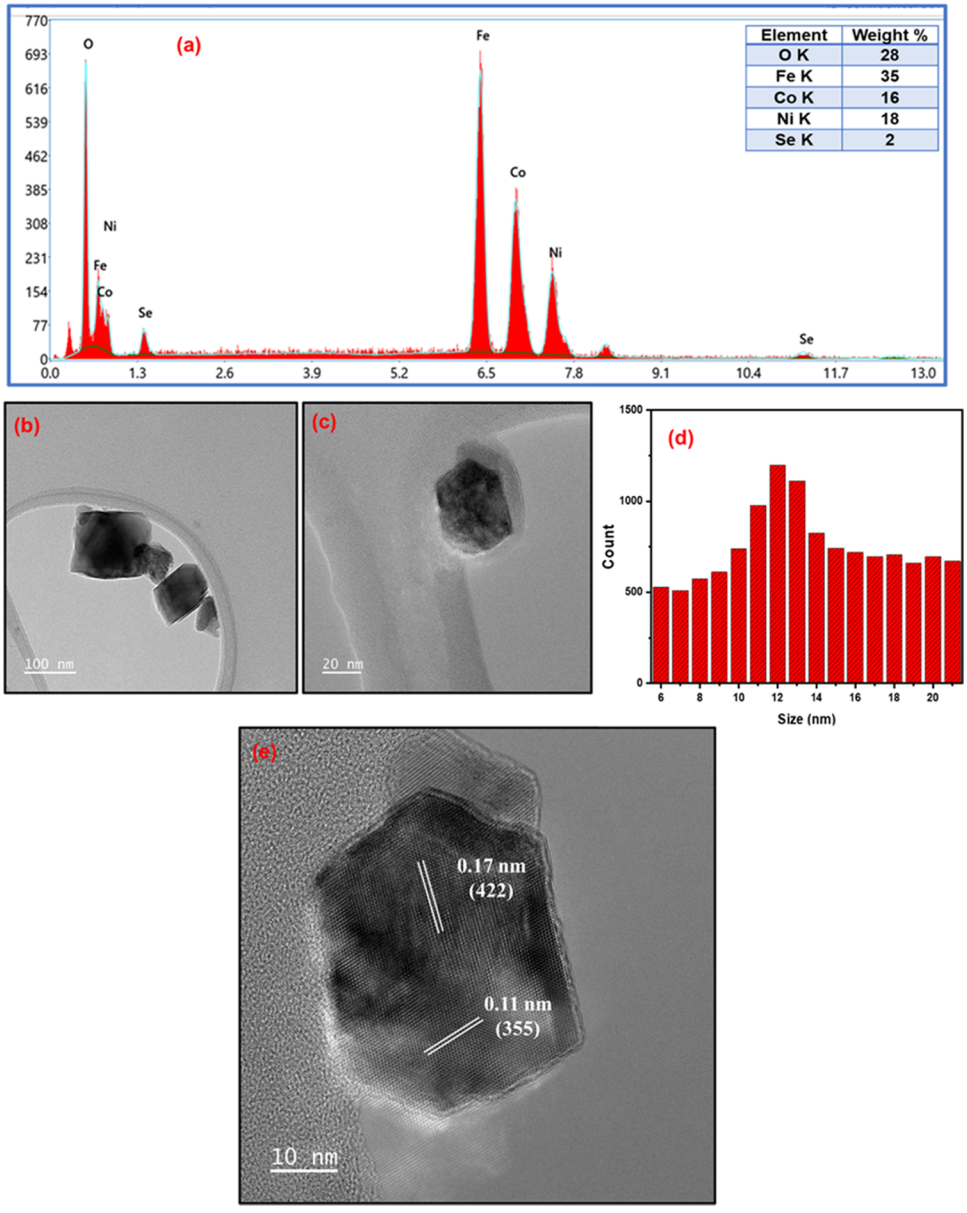

Figure 2. (a) EDX spectrum, (b, c) TEM images, (d) histogram of particle size distribution, and (e) HR-TEM images of CoNi NSFs + x% Se (x = 0.20).

the relevant data is tabulated in Table S3. The maximum magnetization (M_{max}) values at H = 70 kOe range between 32.50 and 41.34 emu/g at RT. The remanent magnetization (M_r) and coercivity (H_c) of the host material ($Co_{0.5}Ni_{0.5}Fe_2O_4$) are 0.78 emu/g and 50.03 Oe, respectively. Those low values denote that the CoNi NSFs without Se suggest a superparamagnetic (SPM)-like behavior at RT. The M_r values of CoNi NSFs + x% Se for x ranging from 0.05 to 0.20 are 17.59, 17.14, 16.84, and 17.16 emu/g. On the other hand, while the H_c of CoNi NSFs + $Se_{x=0.10}$ is 1149.6 Oe, the H_c value remains almost identical, around 1199 Oe for the other samples (with x = 0.05, 0.15, 0.20). Except for the pristine sample, the H_c range refers that CoNi NSFs + x% Se (x = 0.05−0.20) are magnetically hard materials at RT. Magnetic hysteresis loops and the corresponding magnetic parameters at 10 K are presented in Figure 6 and Table S4, respectively. M_{max} and M_r values at 10 K are in the range of 40.17−47.64 emu/g and 27.55−30.53 emu/g, respectively, which are stronger than those at RT, as expected. While the H_c values of CoNi NSFs + x% Se (x = 0.05−0.20) are in the interval of 5000−5250 Oe, the CoNi NSFs without Se (x = 0.00) exhibit a very high H_c (11800.2 Oe) (Figure 6b). In addition to temperature, particle size, shape, and magneto-crystalline anisotropy of the nanoparticles are also key factors in determining the H_c, which governs the magnetic nature of the samples (soft or hard).[29,30] The XRD analysis shows that the average crystal size is in the range of 13−24 nm. The crystallite size plays a crucial role in coercivity and relevant magnetic parameters. For instance, the coercivity can get lower due to the accumulation of particles with larger size.[31] As a result, the size distribution of particles is an important influence on the magnetic properties.[32] Upon incorporation of Se, a dramatic drop in H_c at 10 K can be attributed to the nonuniform particle distribution. The saturation magnetization (M_s) at each temperature is determined through the Stoner−Wohlfarth (S−W) theory.[33,34] To this end, for each sample

https://doi.org/10.1021/acsanm.3c00464
ACS Appl. Nano Mater. XXXX, XXX, XXX−XXX

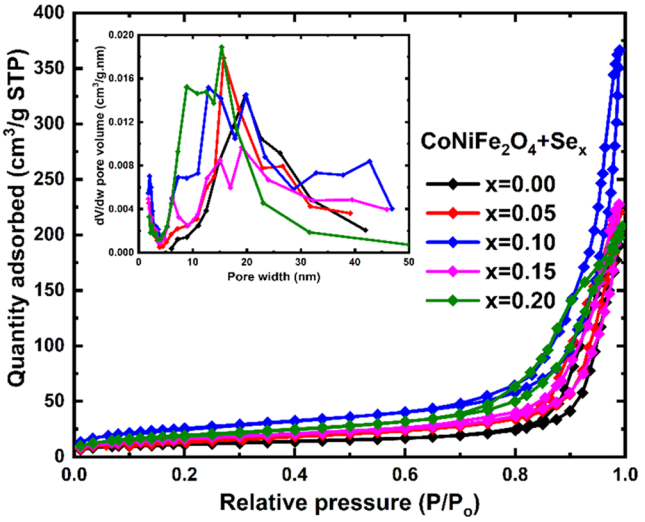

Figure 3. N_2 adsorption−desorption isotherm and pore size distributions of CoNi NSFs (a) x = 0.00, (b) x = 0.05, (c) x = 0.10, (d) x = 0.15, and (e) x = 0.20.

($0.00 \leq x \leq 0.20$), M vs $1/H^2$ variations are extrapolated to zero at each temperature, as shown in Figure 7. The M_s values attained at each temperature are listed in Tables S3 and S4, where M_s becomes the minimum for the host sample (x = 0.0). M_s values for different nanoparticles of CoNi NSFs + x% Se (x = 0.00−0.20) are in the ranges of 33.52−41.93 emu/g at RT and 41.48−49.32 emu/g at 10 K. The incorporation of Se provokes an increment in the M_s of CoNi NSFs + x% Se (x = 0.05−0.20). The highest M_s is observed for CoNi NSFs + $Se_{x=0.10}$ at RT and $CoNiFe_2O_4$ + $Se_{x=0.05}$ at 10 K.

In general, the size, changes in the magnetic moment, local strains, trade interactions, the number of individual sites, and the use of favorite sites all affect the variation of M and associated magnetic parameters.[35,36] The fascinating characteristics of spinel ferrites are chiefly due to the metal cations in the tetrahedral (A) and octahedral (B) sites interacting with each other. These exchange interactions are much more important than those between A−A and B−B. In this context, the dependence of M on H for CoNi NSFs + x% Se (x = 0.00−0.20) is primarily driven by those agents influencing the strength of the A−B interactions. The enhancement of M_{max}, M_s, and M_r with Se compared to those without Se (x = 0.00) can be attributed to reducing the distance separating the magnetic ions, enhancing A−B superexchange interactions. Moreover, a prominent increment in both M_r and H_c with reducing temperature (from RT to 10 K) reflects the reduced thermal fluctuations of magnetic moments.[37]

The magnetic moment (n_B) induced can be calculated through the M_s:[38] $n_B = \frac{M_A \times M_s}{5585}$ where M_A stands for molecular weight. The n_B values of CoNi NSFs + x% Se (x = 0.00−0.20) are found to be in the interval of 1.76 $\mu_B \leq n_B \leq$ 2.26 μ_B and 2.18 $\mu_B \leq n_B \leq$ 2.65 μ_B at RT and 10 K, respectively (Tables S3 and S4). The n_B increases with decreasing temperature for each sample as expected. Besides, the n_B of Se-doped CoNi NSFs is higher than that of undoped CoNi NSFs at each temperature. The enhancement of magnetization with Se (at both RT and 10 K) is pertaining to some major factors: spin pinning at the interface of nanoparticles;[39] upon the incorporation of Se, the increase in the strength of the spin interaction owing to the alteration of bond lengths connecting cations and anions (note that Se modifies the unit cell volume); and the augmentation of spin imbalance due to dissimilar ionic radii of Se and host atoms. Table S1, listing the Rietveld refined structure parameters, demonstrates that the unit cell is getting larger and that the volume enlarges with Se dopant concentration (584.10−590.87 Å^3). The accompanying

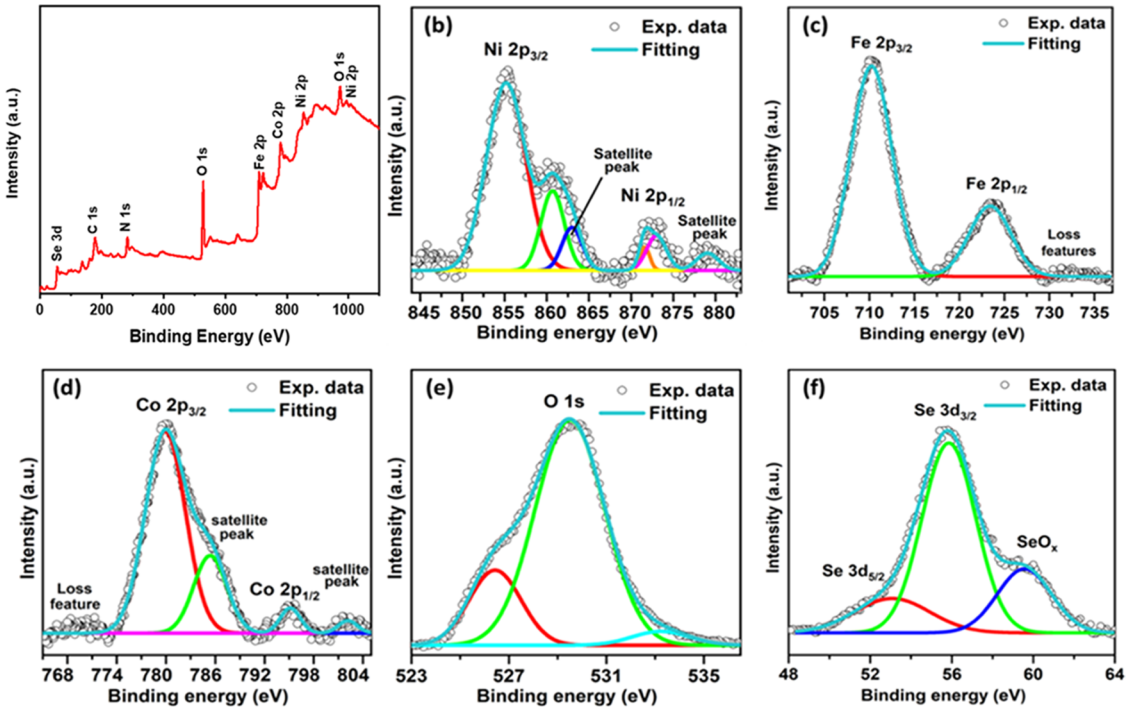

Figure 4. XPS analysis of CoNi NSFs + x% Se with (a) survey scan, and high-resolution spectrum of (b) Ni 2p, (c) Fe 2p, (d) Co 2p, (e) O 1s, and (f) Se 3d.

https://doi.org/10.1021/acsanm.3c00464
ACS Appl. Nano Mater. XXXX, XXX, XXX−XXX

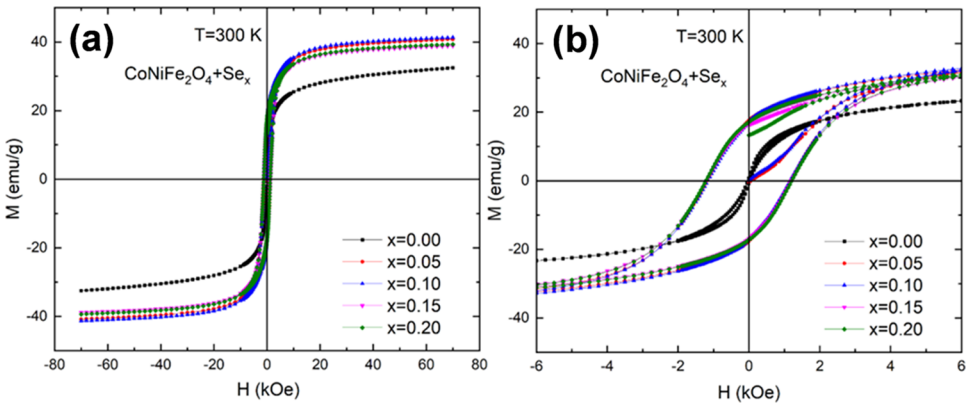

Figure 5. (a) RT M(H) hysteresis loops in an applied field in the range of ±70 kOe. (b) An enlarged view of $M(H)$ curves at RT in the range of −6 kOe ≤ H ≤ + 6 kOe of CoNi NSFs + x% Se (x = 0.00−0.20).

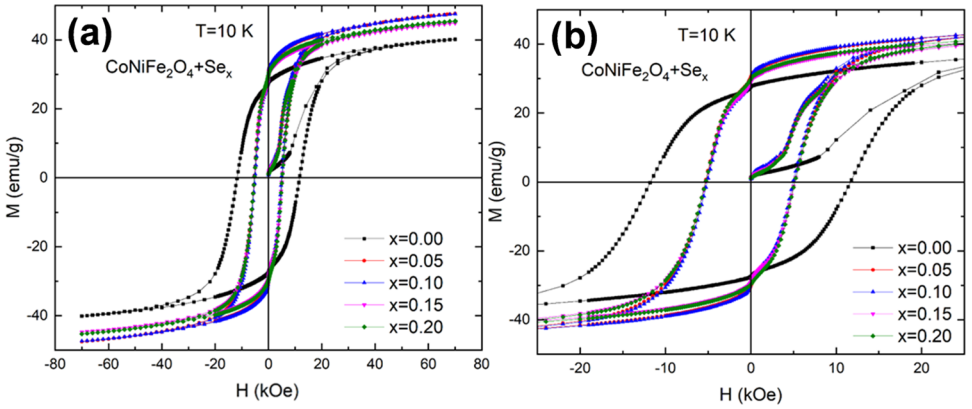

Figure 6. (a) M(H) hysteresis loops measured at 10 K and in an applied field in the range of ±70 kOe. (b) An enlarged view of $M(H)$ curves in the range of −25 kOe ≤ H ≤ + 25 kOe of CoNi NSFs + x% Se (x = 0.00−0.20).

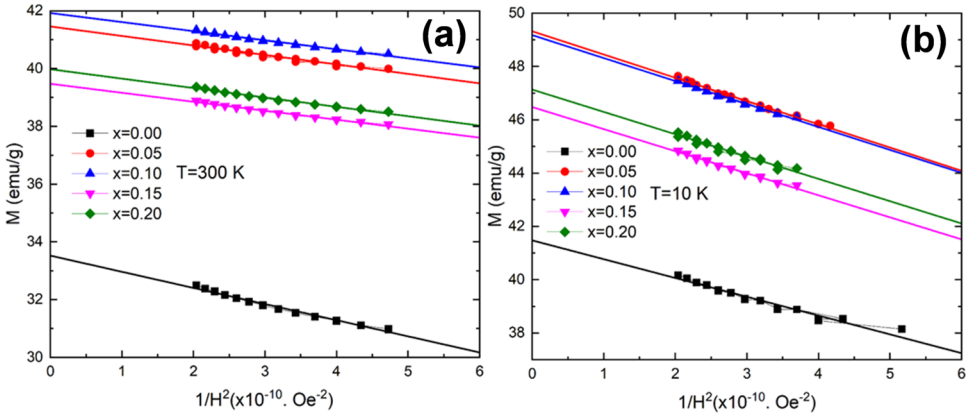

Figure 7. M(H) vs $1/H^2$ at (a) RT and (b) 10 K for CoNi NSFs + x% Se (x = 0.00−0.20).

lattice distortion tunes the magnetic characteristics. The magnetic parameters (Tables S3 and S4) for CoNi NSF + x % Se (x = 0.00−0.20) barely fluctuate, mainly due to scarcely morphological changes. It was already demonstrated that Se could bring about stable electronic states at the surface and contribute to magnetism.[40] Our results indicate that Se can be harnessed to tune the magnetic properties of $Co_{0.5}Ni_{0.5}Fe_2O_4$ nanostructures.

The squareness ratio (a way to measure "squareness" of the hysteresis loop) defined by SQR = M_r/M_s is another important parameter in the magnetic properties. The SQR values of both host and Se-doped samples at RT and 10 K are presented in Tables S3 and S4, respectively. They are in the range of 0.023−0.429 (SQR < 0.5) at RT and 0.601−0.664 (SQR > 0.5) at 10 K. The pristine sample (x = 0.00) displays a very small SQR value lesser than 0.1 at RT, confirming its superparamagnetic behavior at RT. Such observed magnetic behavior could be attributed to the very small crystallites/particle size that is comparable (or lesser) to the critical superparamagnetic domain size.[41] Indeed, it is reported that $CoFe_2O_4$ nanoparticles display a critical superparamagnetic domain size of about 10 nm. In the present investigation, XRD results

https://doi.org/10.1021/acsanm.3c00464
ACS Appl. Nano Mater. XXXX, XXX, XXX−XXX

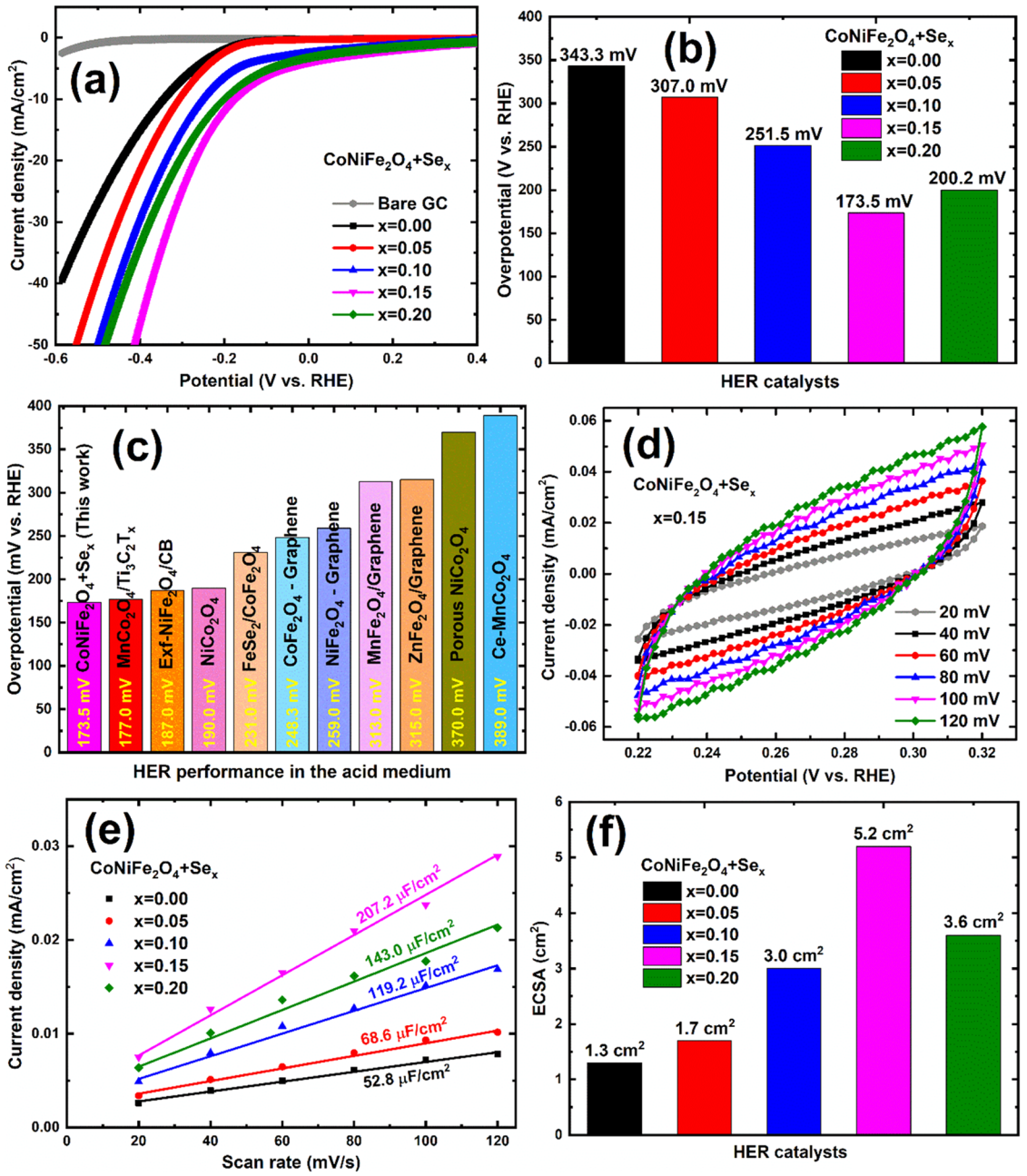

Figure 8. (a) LSV polarization curves, (b) normalized overpotential histograms, (c) HER performance comparison in literatures, (d) CV curve, (e) C_{dl} plots, and (f) ECSA histograms of CoNi NSFs + x% Se (x = 0.00−0.20).

revealed that the pristine sample has a D_{XRD} value of about 13 nm that is comparable to the mentioned critical superparamagnetic domain size, confirming the observed superparamagnetic behavior in the pristine sample at RT. The remaining samples showed SQR values around 0.40−0.42 at RT, implying the formation of a single domain structure with uniaxial symmetry.[33] An SQR value less than 0.5 can be ascribed to the influence of a surface spin disorder. An SQR higher than 0.5 designates the creation of multimagnetic domains and reflects one of the major characteristics of hard nanocomposite magnets. In the present work, SQR > 0.5 is observed for all samples at 10 K. The present findings are consistent with the results observed for Se-doped Bi ferrite nanosheets.[42]

Evaluation of HER Activity. The electrocatalytic HER measurements were conducted in 0.5 M H_2SO_4 solution with pH = 0.3 using CoNi NSFs + x% Se (x = 0.00−0.20) as a cathode. LSV (linear sweep voltammetry) was applied to study how the current was varied across a certain range of potentials for HER during CoNi NSFs + x% Se (x = 0.00−0.20) optimization at the GC electrode. The LSV curves for all catalysts taken at the same scan rate of 10 mV/s are depicted in Figure 8a. Compared to Se-doped CoNi electrodes, the undoped CoNi demonstrated poor HER performance with large overpotential (i.e., 343.5 mV) at a 10 mA/cm^2 current density. The catalytic activity for HER is significantly enhanced in the case of % Se (x = 0.15) doped into the CoNi matrix and reached 173.5 mV with a 170 mV anodic shift from the bare CoNi electrode at a 10 mA/cm^2 overpotential (Figure 8a).

https://doi.org/10.1021/acsanm.3c00464
ACS Appl. Nano Mater. XXXX, XXX, XXX−XXX

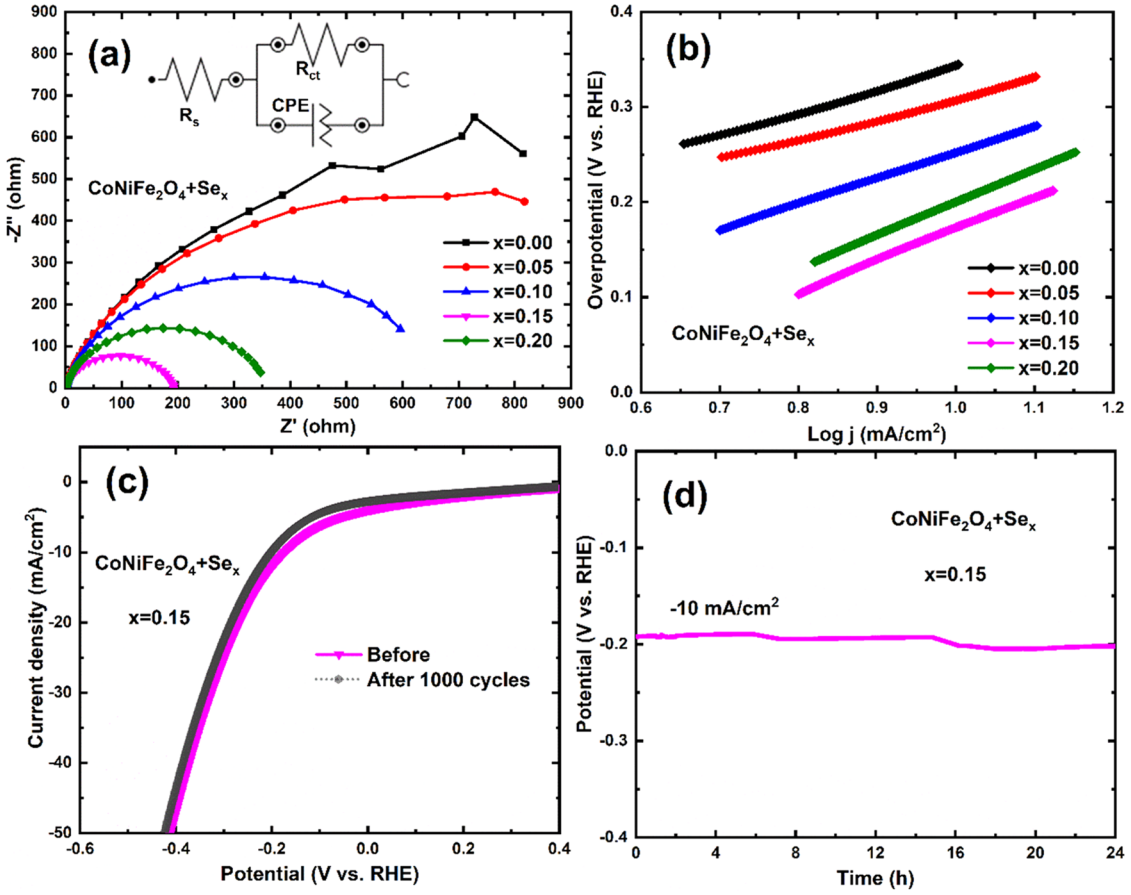

Figure 9. (a) EIS plots, (b) Tafel plots, (c) stability test curves, and (d) chronopotentiometry curves of CoNi NSFs + *x*% Se (*x* = 0.15).

The higher ratio of % Se (*x* = 0.15) in the CoNi matrix suppresses the catalytic HER activity, which might be related to the aggregation generated by the greater concentration of Se, which tends to decrease the HER performance. For better understanding, the overpotential histogram of different electrodes at −10 mA/cm^2 is shown in Figure 8b. The performance of CoNi NSFs + *x*% Se (*x* = 0.15) as an electrocatalyst for HER was compared to that of other HER catalysts reported in the literature[43−52] as shown in Figure 8c.

The electrochemically active surface area (ECSA) was assessed to confirm the assumption that CoNi NSFs + *x*% Se (*x* = 0.15) has a significant impact on the improved performance of HER. The ECSA can be extracted from double-layer capacitance (C_{dl})[53] by measuring the CVs from 20 to 120 mV/s scan rates (Figures 8d and S1), and calculating the C_{dl} value is shown in Figure 8e. The ECSA plots for all catalysts are depicted in Figure 8f. For instance, an ESCA of 1.3, 1.7, 3.0, 5.2, and 3.6 cm^2 is required for CoNi NSFs + *x*% Se (*x* = 0.00−0.20) electrodes. Compared to Se-doped CoNi electrodes, the undoped CoNi demonstrated poor HER performance due to the low ECSA of 1.3 cm^2. Increasing the Se-doped concentration on the CoNi matrix enhances the ECSA and reaches 5.2 cm^2 in the case of % Se (*x* = 0.15) doped into the CoNi matrix. After that, the ECSA is reduced as the concentration of Se doped into the CoNi matrix increases. It could be because the Se is covering up the active sites of the CoNi matrix and making more recombination centers instead of making more active sites. This indicates that CoNi NSFs + *x* % Se (*x* = 0.15) electrode has a high ECSA, which is responsible for higher electrode activity for HER. Table S5 shows the calculated typical HER parameters (overpotential, Tafel slope, ECSA) of the CoNi NSFs + *x*% Se (*x* = 0.00−0.20) for more clarity under comparable circumstances.

As shown in Figure 9a, the EIS analysis was performed to comprehend the catalyst's efficacy in the charge transporting at the semiconductor electrolyte interface (SEI) in a 0.5 M H_2SO_4 electrolyte solution. The electron transfer at SEI occurs quickly and strongly in the tiny semicircle, suggesting significant electrocatalytic activity.[54] The Nyquist plot of CoNi NSFs + *x*% Se (*x* = 0.00−0.20) was measured at an overpotential of 173.5 mV, and frequencies range from 0.1 to 10^5 Hz, as depicted in Figure 9a. The inset of Figure 9a shows a simulation of the equivalent circuit, where R_S and R_{ct} are the resistance of the electrolyte solution and resistance of the charge-transfer electrolyte interface, respectively.[55,56] Also, the CoNi NSFs + *x*% Se (*x* = 0.15) electrocatalyst with the smallest arc radius had a lower charge-transfer resistance than other catalysts. This showed that it greatly improved the performance of the HER and was consistent with the results observed in Figure 8a.

Moreover, the Tafel plot was measured to get more insight into the electrocatalytic kinetics for HER by *x*% Se doping (*x* = 0.00−0.20) into the CoNi matrix, as shown in Figure 9b. The slope of catalysts was determined using the Tafel relation ($\eta = b \log(j) + a$, where η, j, b, and a denote overpotential, current density, slope, and constant, respectively).[57] The calculated Tafel slope of CoNi NSFs + *x*% Se (*x* = 0.00−0.20) catalysts exhibits slopes ranging from 91 to 162 mV/dec. The Tafel slope values of the CoNi NSFs + *x*% Se (*x* = 0.15) electrocatalyst were as low as 91 mV/dec, which supports

https://doi.org/10.1021/acsanm.3c00464
ACS Appl. Nano Mater. XXXX, XXX, XXX−XXX

the assumption that this material follows the Volmer–Heyrovsky rate-determining step in HER. In general, when an acidic medium performs HER, three primary processes are at work as follows: the Tafel process (30 mV/dec), the Heyrovsky process (40 mV/dec), and the Volmer process (120 mV/dec), respectively. In the first stage, which is called the Volmer reaction, the hydrogen atom absorbs a proton that has been released from the electrode surface. In the Heyrovsky process, H_{ads} will merge with a proton and an electron to create hydrogen molecules. The Tafel process suggests recombining two H_{ads} species to create molecules of hydrogen. The Volmer–Heyrovsky route involves the Volmer and Heyrovsky processes and is the most common way for the HER mechanism to proceed.[54,58] The estimated Tafel slope of 91 mV/dec for the most effective electrocatalyst CoNi NSFs + x% Se (x = 0.00–0.20) shows that the reaction goes through the rate-determining Volmer–Heyrovsky step.

In addition to HER activity, electrocatalyst performance may be assessed in the essential features of its stability.[58] According to the results above, a CoNi NSFs + x% Se (x = 0.15) electrode may be employed realistically for electrocatalytic hydrogen evolution applications. The findings of employing the chronopotentiometry (CP) method to access the stability of the CoNi NSFs + x% Se (x = 0.15) in a 0.5 M H_2SO_4 solution at 10 mA/cm^2 are shown in Figure 9d. The horizontal line in the graph depicts the exceptional stability of the Se-doped CoNi NSF catalyst over a 24 h period. Further, as indicated in Figure 9c, the LSV stability studies were performed after 1000 cycles. The LSV of the CoNi NSFs + x% Se (x = 0.15) catalyst shifted around 5 mV, which might diminish the electrochemically active surface area affected by the accumulation of ions in the pores of the catalyst.

CONCLUSIONS

In summary, CoNi NSFs + x% Se (x = 0.00–0.20) were prepared successfully using a sol–gel autocombustion method followed by an advanced green laser ablation technique. The synthesized materials were characterized by XRD, SEM equipped with EDX, TEM, HR-TEM, and XPS analyses for their structural, morphological, and chemical compositions. $M(H)$ curves and associated magnetic parameters demonstrate that Se plays a significant role in the magnetic characteristics of the pristine $Co_{0.5}Ni_{0.5}Fe_2O_4$ sample. The pristine sample showed superparamagnetic-like nature at RT. However, the pristine sample at 10 K and all Se-doped samples (x = 0.05–0.20) at both RT and 10 K illustrated hard ferromagnetic behavior. For all samples, magnetic parameters are enhanced with a Se concentration of x = 0.05 at RT. They barely fluctuate for samples with $0.05 \leq x \leq 0.20$ at both RT and 10 K, which can be attributed to the rare morphological changes. High SQR values (SQR > 0.5) achieved at 10 K allude to the high coercivity at low temperatures and indicate forming of a multimagnetic domain structure. At room temperature, an abrupt increment in the SQR once Se is added to the host sample shows the enormous effect of Se on remanence. Our results demonstrate that Se could be a promising dopant to tailor the magnetic properties of CoNi NSFs. Additional benefits can be derived from the magnetism of these advanced catalysts. The CoNi NSFs + x% Se (x = 0.15) electrode has excellent HER activity much better than its other catalysts. The optimized catalyst CoNi NSFs + x% Se (x = 0.15) electrode needs a low overpotential of 173.5 mV at 10 mA/cm^2 and a low Tafel slope of 91 mV/dec in a 0.5 M H_2SO_4 electrolyte. The remarkable performance of CoNi NSFs + x% Se (x = 0.15) is owing to the ECSA and electron transport capacity at the electrode/electrolyte interface. Further, the long-term analysis of CoNi NSFs + x% Se (x = 0.15) electrode materials is highly stable even after 1000 CV cycles and 24 h of CP testing. These results revealed that CoNi NSFs + x% Se (x = 0.15) could be a promising candidate electrode material for the electrochemical hydrogen evolution. This work provides innovative guidance for the design and synthesis of heterostructure catalysts for electrochemical hydrogen production in practical applications. While also this work adds to the basic understanding of magnetic field-induced electrochemical reactions, which may open new avenues of research in the field of magnetoelectrochemistry in the future.

ASSOCIATED CONTENT

Data Availability Statement

The data sets used and/or analyzed during the current study are available from the corresponding author on reasonable request.

Supporting Information

The Supporting Information is available free of charge at https://pubs.acs.org/doi/10.1021/acsanm.3c00464.

Materials and methods, synthesis of CoNi NSFs + x% Se (x = 0.00–0.20), material characterization, W–H plots of CoNi NSFs + x% Se (x = 0.00–0.20), SEM micrographs of CoNi NSFs + x% Se (x = 0.00–0.20), FTIR spectra of CoNi NSFs + x% Se (x = 0.00–0.20), CV polarization curves of the various CoNi NSFs + x% Se (x = 0.00–0.20), Rietveld refined structure parameters of CoNi NSFs + x% Se (x = 0.00–0.20), surface area and pore size distribution properties of CoNi NSFs + x% Se (x = 0.00–0.20), magnetic parameters of CoNi NSFs + x% Se (x = 0.00–0.20) at RT, magnetic parameters of CoNi NSFs + x% Se (x = 0.00–0.20) at 10 K, and HER parameters of CoNi NSFs + x% Se (x = 0.00–0.20) (PDF)

AUTHOR INFORMATION

Corresponding Authors

Mohammed Ashraf Gondal – *Laser Research Group, Department of Physics & Interdisciplinary Research Center for Hydrogen and Energy Storage (IRC-HES), King Fahd University of Petroleum and Minerals (KFUPM), Dhahran 31261, Saudi Arabia; K. A. CARE Energy Research and Innovation Center, King Fahd University of Petroleum and Minerals, Dhahran 31261, Saudi Arabia;* orcid.org/0000-0001-9570-4569; Email: magondal@kfupm.edu.sa

Anurag Roy – *Solar Energy Research Group, Environment and Sustainability Institute, University of Exeter, Penryn Campus, Cornwall TR10 9FE, U.K.;* orcid.org/0000-0002-2097-9442; Email: A.Roy30@exeter.ac.uk

Authors

Mohamed Jaffer Sadiq Mohamed – *Laser Research Group, Department of Physics & Interdisciplinary Research Center for Hydrogen and Energy Storage (IRC-HES), King Fahd University of Petroleum and Minerals (KFUPM), Dhahran 31261, Saudi Arabia*

Serkan Caliskan – *Department of Physical and Applied Sciences, University of Houston-Clear Lake, Houston, Texas 77058, United States*

https://doi.org/10.1021/acsanm.3c00464
ACS Appl. Nano Mater. XXXX, XXX, XXX–XXX

Munirah Abdullah Almessiere − *Department of Biophysics, Institute for Research and Medical Consultations (IRMC), Imam Abdulrahman Bin Faisal University, Dammam 31441, Saudi Arabia; Department of Physics, College of Science, Imam Abdulrahman Bin Faisal University, Dammam 31441, Saudi Arabia;* orcid.org/0000-0003-1651-3591

Abdulhadi Baykal − *Department of Nanomedicine Research, Institute for Research and Medical Consultations (IRMC), Imam Abdulrahman Bin Faisal University, Dammam 31441, Saudi Arabia*

Yassine Slimani − *Department of Biophysics, Institute for Research and Medical Consultations (IRMC), Imam Abdulrahman Bin Faisal University, Dammam 31441, Saudi Arabia;* orcid.org/0000-0002-2579-1617

Khaled Abdelsabour Elsayed − *Department of Basic Engineering Sciences, College of Engineering, Imam Abdulrahman Bin Faisal University, Dammam 31441, Saudi Arabia*

Muhammad Hassan − *Laser Research Group, Department of Physics & Interdisciplinary Research Center for Hydrogen and Energy Storage (IRC-HES), King Fahd University of Petroleum and Minerals (KFUPM), Dhahran 31261, Saudi Arabia; School of Physics, Minhaj University Lahore, Punjab 54000, Pakistan;* orcid.org/0000-0002-5846-695X

Ismail Abdullah Auwal − *Department of Chemistry, Faculty of Natural and Applied Sciences, Sule Lamido University, PMB 048 Kafin Hausa, Jigawa State, Nigeria*

Abdul Zeeshan Khan − *Department of Chemistry, Forman Christian College, Lahore 54600, Pakistan*

Asif Ali Tahir − *Solar Energy Research Group, Environment and Sustainability Institute, University of Exeter, Penryn Campus, Cornwall TR10 9FE, U.K.;* orcid.org/0000-0003-1985-6127

Complete contact information is available at: https://pubs.acs.org/10.1021/acsanm.3c00464

Author Contributions

M.J.S.M., M.A.A., and A.B.: conceptualization and design of the work, investigation, writing, and explaining electrochemical hydrogen evolution reaction, and writing—review and editing. S.C. and Y.S.: investigation, writing, and explaining structure and magnetic properties, writing—review and editing. M.H., I.A.A., and A.Z.K.: formal analysis, data curation, and validation. K.A.E. and A.A.T.: writing—review and editing. M.A.G. and A.R.: supervision, conceptualization, writing—review and editing, project administration, and funding acquisition.

Notes

The authors declare no competing financial interest.

■ ACKNOWLEDGMENTS

M.A.G. and A.R. acknowledge the UK-Saudi challenge fund program 2022 sponsored by British Council. M.A.A., A.B., and Y.S. acknowledged the Institute for Research and Medical Consultations of Imam Abdulrahman Bin Faisal University (Dammam, Saudi Arabia) for providing laboratory facilities. K.A.E. acknowledges the College of Engineering, Imam Abdulrahman Bin Faisal University (Dammam, Saudi Arabia) for using the laser laboratory. M.J.S.M. acknowledges the King Fahd University of Petroleum and Minerals, Dhahran, Saudi Arabia, for providing a postdoctoral fellowship under Distinguished Professorship Award # DUP18101. M.A.G. is thankful to K.A. CARE for the Senior Research Fellowship and KFUPM for supporting this work under project # INHE 2211.

■ REFERENCES

(1) Ramzan, M.; Raza, S. A.; Usman, M.; Sharma, G. D.; Iqbal, H. A. Environmental Cost of Non-Renewable Energy and Economic Progress: Do ICT and Financial Development Mitigate Some Burden? *J. Cleaner Prod.* **2022**, *333*, No. 130066.

(2) Belhadj, H.; Messaoudi, Y.; Khelladi, M. R.; Azizi, A. A Facile Synthesis of Metal Ferrites (MFe_2O_4, M = Co, Ni, Zn, Cu) as Effective Electrocatalysts toward Electrochemical Hydrogen Evolution Reaction. *Int. J. Hydrogen Energy* **2022**, *47*, 20129−20137.

(3) Qureshi, F.; Yusuf, M.; Kamyab, H.; Vo, D.-V. N.; Chelliapan, S.; Joo, S.-W.; Vasseghian, Y. Latest Eco-Friendly Avenues on Hydrogen Production towards a Circular Bioeconomy: Currents Challenges, Innovative Insights, and Future Perspectives. *Renewable Sustainable Energy Rev.* **2022**, *168*, No. 112916.

(4) Huang, Y.; Tian, F.; Liu, Y.; Li, M.; Xu, S.; Yu, Y.; Li, J.; Yang, W.; Li, H. Mesoporous Cobalt Ferrite Phosphides/Reduced Graphene Oxide as Highly Effective Electrocatalyst for Overall Water Splitting. *J. Colloid Interface Sci.* **2022**, *605*, 667−673.

(5) Hou, X.; Zhou, H.; Zhao, M.; Cai, Y.; Wei, Q. MoS_2 Nanoplates Embedded in Co-N-Doped Carbon Nanocages as Efficient Catalyst for HER and OER. *ACS Sustainable Chem. Eng.* **2020**, *8*, 5724−5733.

(6) Zahra, R.; Pervaiz, E.; Yang, M.; Rabi, O.; Saleem, Z.; Ali, M.; Farrukh, S. A Review on Nickel Cobalt Sulphide and Their Hybrids: Earth Abundant, PH Stable Electro-Catalyst for Hydrogen Evolution Reaction. *Int. J. Hydrogen Energy* **2020**, *45*, 24518−24543.

(7) Rafeeq, H.; Hussain, A.; Ambreen, A.; Waqas, M.; Bilal, M.; Iqbal, H. M. N. Functionalized Nanoparticles and Their Environmental Remediation Potential: A Review. *J. Nanostruct. Chem.* **2022**, *12*, 1007−1031.

(8) Almessiere, M. A.; Slimani, Y. A.; Hassan, M.; Gondal, M. A.; Cevik, E.; Baykal, A. Investigation of Hard/Soft $CoFe_2O_4$/$NiSc_{0.03}Fe_{1.97}O_4$ Nanocomposite for Energy Storage Applications. *Int. J. Energy Res.* **2021**, *45*, 16691−16708.

(9) Ahmed, I.; Khan, A. N.; Jan, R.; Gul, I. H. Structure−Properties Relationships of Graphene and Spinel Nickel Ferrites Based Poly (Vinylidene Fluoride) Hybrid Polymer Nanocomposites for Improved Dielectric and EMI Shielding Characteristics. *Mater. Res. Bull.* **2022**, *148*, No. 111687.

(10) Srinivasan, S. Y.; Paknikar, K. M.; Bodas, D.; Gajbhiye, V. Applications of Cobalt Ferrite Nanoparticles in Biomedical Nanotechnology. *Nanomedicine* **2018**, *13*, 1221−1238.

(11) Deng, X.; Sorescu, D. C.; Waluyo, I.; Hunt, A.; Kauffman, D. R. Bulk vs Intrinsic Activity of NiFeOx Electrocatalysts in the Oxygen Evolution Reaction: The Influence of Catalyst Loading, Morphology, and Support Material. *ACS Catal* **2020**, *10*, 11768−11778.

(12) Lone, G. A.; Ikram, M. Role of Ni Doping in Magnetic Dilution of Fe Sublattice and in Tailoring Optical Properties of $CoFe_2O_4$. *J. Alloys Compd.* **2023**, *934*, No. 167891.

(13) Chen, C.; Tuo, Y.; Lu, Q.; Lu, H.; Zhang, S.; Zhou, Y.; Zhang, J.; Liu, Z.; Kang, Z.; Feng, X.; Chen, D. Hierarchical Trimetallic Co-Ni-Fe Oxides Derived from Core-Shell Structured Metal-Organic Frameworks for Highly Efficient Oxygen Evolution Reaction. *Appl. Catal., B* **2021**, *287*, No. 119953.

(14) Abbas, N.; Rubab, N.; Sadiq, N.; Manzoor, S.; Khan, M. I.; Fernandez Garcia, J.; Barbosa Aragao, I.; Tariq, M.; Akhtar, Z.; Yasmin, G. Aluminum-Doped Cobalt Ferrite as an Efficient Photocatalyst for the Abatement of Methylene Blue. *Water* **2020**, *12*, No. 2285.

(15) Umar, M.; Mahmood, N.; Awan, S. U.; Fatima, S.; Mahmood, A.; Rizwan, S. Rationally Designed La and Se Co-Doped Bismuth Ferrites with Controlled Bandgap for Visible Light Photocatalysis. *RSC Adv.* **2019**, *9*, 17148−17156.

(16) Slimani, Y.; Almessiere, M. A.; Korkmaz, A. D.; Baykal, A.; Gungunes, H.; Vakhitov, M. G.; Klygach, D. S.; Trukhanov, Sv.; Trukhanov, Av. The Impact of Indium Ion on Structural, Magnetic,

and Electrodynamic Traits of Co-Ni Nanospinel Ferrites. *J. Magn. Magn. Mater.* **2022**, *562*, No. 169782.
(17) Hassan, M.; Slimani, Y.; Gondal, M. A.; Mohamed, M. J. S.; Guener, S.; Almessiere, M. A.; Surrati, A. M.; Baykal, A.; Trukhanov, S.; Trukhanov, A. Structural Parameters, Energy States and Magnetic Properties of the Novel Se-Doped $NiFe_2O_4$ Ferrites as Highly Efficient Electrocatalysts for HER. *Ceram. Int.* **2022**, *48*, 24866−24876.
(18) Li, G.; Yin, F.; Lei, Z.; Zhao, X.; He, X.; Li, Z.; Yu, X. Se-Doped Cobalt Oxide Nanoparticle as Highly-Efficient Electrocatalyst for Oxygen Evolution Reaction. *Int. J. Hydrogen Energy* **2022**, *47*, 216−227.
(19) Maksoud, M. I. A. A.; El-ghandour, A.; El-Sayyad, G. S.; Awed, A. S.; Fahim, R. A.; Atta, M. M.; Ashour, A. H.; El-Batal, A. I.; Gobara, M.; Abdel-Khalek, E. K.; El-Okr, M. M. Tunable Structures of Copper Substituted Cobalt Nanoferrites with Prospective Electrical and Magnetic Applications. *J. Mater. Sci. Mater.: Electron.* **2019**, *30*, 4908−4919.
(20) Bhujun, B.; Tan, M. T. T.; Shanmugam, A. S. Evaluation of Aluminium Doped Spinel Ferrite Electrodes for Supercapacitors. *Ceram. Int.* **2016**, *42*, 6457−6466.
(21) Baykal, A.; Kasapoğlu, N.; Köseoğlu, Y.; Toprak, M. S.; Bayrakdar, H. CTAB-Assisted Hydrothermal Synthesis of $NiFe_2O_4$ and Its Magnetic Characterization. *J. Alloys Compd.* **2008**, *464*, 514−518.
(22) Zaki, H. M.; Dawoud, H. A. Far-Infrared Spectra for Copper−Zinc Mixed Ferrites. *Phys. B* **2010**, *405*, 4476−4479.
(23) Abd El-Lateef, H. M.; Khalaf, M. M.; Alnajjar, A. O.; Mohamed, I. M. A. Facile Synthesis of Co/Ni Bimetallic Phosphate as Electrode Material for Urea Fuel Cells: Effect of Synthetic Strategy on the Physicochemical and Electrocatalytic Behavior. *Fuel* **2023**, *334*, No. 126671.
(24) Qu, L.; Wang, Z.; Hou, X.; Mao, J.; Wang, S.; Sun, G.; Wu, Y.; Liu, X. "Rose Flowers" Assembled from Mesoporous $NiFe_2O_4$ Nanosheets for Energy Storage Devices. *J. Mater. Sci. Mater.: Electron.* **2017**, *28*, 14058−14068.
(25) Zhang, Z.; Li, W.; Zou, R.; Kang, W.; San Chui, Y.; Yuen, M. F.; Lee, C.-S.; Zhang, W. Layer-Stacked Cobalt Ferrite ($CoFe_2O_4$) Mesoporous Platelets for High-Performance Lithium Ion Battery Anodes. *J. Mater. Chem. A: Mater.* **2015**, *3*, 6990−6997.
(26) Wu, L. Q.; Li, Y. C.; Li, S. Q.; Li, Z. Z.; Tang, G. D.; Qi, W. H.; Xue, L. C.; Ge, X. S.; Ding, L. L. Method for Estimating Ionicities of Oxides Using O1s Photoelectron Spectra. *AIP Adv.* **2015**, *5*, No. 097210.
(27) Dupin, J. C.; Gonbeau, D.; Vinatier, P.; Levasseur, A. Systematic XPS Studies of Metal Oxides, Hydroxides and Peroxides. *Phys. Chem. Chem. Phys.* **2000**, *2*, 1319−1324.
(28) Jiang, Q. S.; Li, W.; Wu, J.; Cheng, W.; Zhu, J.; Yan, Z.; Wang, X.; Ju, Y. Electrodeposited Cobalt and Nickel Selenides as High-Performance Electrocatalytic Materials for Dye-Sensitized Solar Cells. *J. Mater. Sci. Mater.: Electron.* **2019**, *30*, 9429−9437.
(29) Slimani, Y.; Almessiere, M. A.; Nawaz, M.; Baykal, A.; Akhtar, S.; Ercan, I.; Belenli, I. Effect of Bimetallic (Ca, Mg) Substitution on Magneto-Optical Properties of $NiFe_2O_4$ Nanoparticles. *Ceram. Int.* **2019**, *45*, 6021−6029.
(30) al Khabouri, S.; al Harthi, S.; Maekawa, T.; Nagaoka, Y.; Elzain, M. E.; al Hinai, A.; Al-Rawas, A. D.; Gismelseed, A. M.; Yousif, A. A. Composition, Electronic and Magnetic Investigation of the Encapsulated $ZnFe_2O_4$ Nanoparticles in Multiwall Carbon Nanotubes Containing Ni Residuals. *Nanoscale Res. Lett.* **2015**, *10*, No. 262.
(31) Ghunaim, R.; Scholz, M.; Damm, C.; Rellinghaus, B.; Klingeler, R.; Büchner, B.; Mertig, M.; Hampel, S. Single-Crystalline FeCo Nanoparticle-Filled Carbon Nanotubes: Synthesis, Structural Characterization and Magnetic Properties. *Beilstein J. Nanotechnol.* **2018**, *9*, 1024−1034.
(32) Zhao, L.; Yang, H.; Cui, Y.; Zhao, X.; Feng, S. Study of Preparation and Magnetic Properties of Silica-Coated Cobalt Ferrite Nanocomposites. *J. Mater. Sci.* **2007**, *42*, 4110−4114.
(33) Stoner, E. C.; Wohlfarth, E. P. A Mechanism of Magnetic Hysteresis in Heterogeneous Alloys. *Philos. Trans. R. Soc., A* **1948**, *240*, 599−642.
(34) Atherton, D. L.; Beattie, J. R. A Mean Field Stoner-Wohlfarth Hysteresis Model. *IEEE Trans. Magn.* **1990**, *26*, 3059−3063.
(35) Almessiere, M. A.; Slimani, Y.; Ali, S.; Baykal, A.; Ercan, I.; Sozeri, H. Nd3+ Ion-Substituted $Co_{1-2x}Ni_xMn_xFe_{2-Y}Nd_yO_4$ Nanoparticles: Structural, Morphological, and Magnetic Investigations. *J. Inorg. Organomet. Polym. Mater.* **2019**, *29*, 783−791.
(36) Slimani, Y.; Güngüneş, H.; Nawaz, M.; Manikandan, A.; el Sayed, H. S.; Almessiere, M. A.; Sözeri, H.; Shirsath, S. E.; Ercan, I.; Baykal, A. Magneto-Optical and Microstructural Properties of Spinel Cubic Copper Ferrites with Li-Al Co-Substitution. *Ceram. Int.* **2018**, *44*, 14242−14250.
(37) Almessiere, M. A.; Slimani, Y.; Baykal, A. Structural and Magnetic Properties of Ce-Doped Strontium Hexaferrite. *Ceram. Int.* **2018**, *44*, 9000−9008.
(38) Korkmaz, A. D.; Güner, S.; Slimani, Y.; Gungunes, H.; Amir, M.; Manikandan, A.; Baykal, A. Microstructural, Optical, and Magnetic Properties of Vanadium-Substituted Nickel Spinel Nanoferrites. *J. Supercond. Nov. Magn.* **2019**, *32*, 1057−1065.
(39) Berkowitz, A. E.; Lahut, J. A.; Jacobs, I. S.; Levinson, L. M.; Forester, D. W. Spin Pinning at Ferrite-Organic Interfaces. *Phys. Rev. Lett.* **1975**, *34*, 594.
(40) Pal, A.; Shirodkar, S. N.; Gohil, S.; Ghosh, S.; Waghmare, Uv.; Ayyub, P. Multiferroic Behavior in Elemental Selenium below 40 K: Effect of Electronic Topology. *Sci. Rep.* **2013**, *3*, No. 2051.
(41) Slimani, Y.; Guner, S.; Almessiere, M. A.; Hannachi, E.; Manikandan, A.; Baykal, A. Magnetic Characterization of Nanomaterials. In *Synthesis and Applications of Nanoparticles*; Springer, 2022; pp 177−238.
(42) Rizwan, S.; Umar, M.; Babar, Z. U. D.; Awan, S. U.; ur Rehman, M. A. Selenium-Enriched Flower-like of Bismuth Ferrite Nanosheets Assembly with Associated Magnetic Properties. *AIP Adv.* **2019**, *9*, No. 055025.
(43) Huang, H.; Shen, B.; Yan, M.; He, H.; Yang, L.; Jiang, Q.; Ying, G. Coupled Spinel Manganese− Cobalt Oxide and MXene Electrocatalysts towards Efficient Hydrogen Evolution Reaction. *Fuel* **2022**, *328*, No. 125234.
(44) Munonde, T. S.; Zheng, H.; Matseke, M. S.; Nomngongo, P. N.; Wang, Y.; Tsiakaras, P. A Green Approach for Enhancing the Electrocatalytic Activity and Stability of $NiFe_2O_4$/CB Nanospheres towards Hydrogen Production. *Renewable Energy* **2020**, *154*, 704−714.
(45) Liu, D.; Zhang, C.; Yu, Y.; Shi, Y.; Yu, Y.; Niu, Z.; Zhang, B. Hydrogen Evolution Activity Enhancement by Tuning the Oxygen Vacancies in Self-Supported Mesoporous Spinel Oxide Nanowire Arrays. *Nano Res* **2018**, *11*, 603−613.
(46) Zhang, H.; Nengzi, L.; Li, B.; Cheng, Q.; Gou, J.; Cheng, X. Successfully Synthesis of $FeSe_2/CoFe_2O_4$ Heterojunction with High Performance for Hydrogen Evolution Reaction. *Renewable Energy* **2020**, *155*, 717−724.
(47) Nivetha, R.; Chella, S.; Kollu, P.; Jeong, S. K.; Bhatnagar, A.; Andrews, N. G. Cobalt and Nickel Ferrites Based Graphene Nanocomposites for Electrochemical Hydrogen Evolution. *J. Magn. Magn. Mater.* **2018**, *448*, 165−171.
(48) Nivetha, R.; Grace, A. N. Manganese and Zinc Ferrite Based Graphene Nanocomposites for Electrochemical Hydrogen Evolution Reaction. *J. Alloys Compd.* **2019**, *796*, 185−195.
(49) Elakkiya, R.; Ramkumar, R.; Maduraiveeran, G. Flower-like Nickel-Cobalt Oxide Nanomaterials as Bi-Functional Catalyst for Electrochemical Water Splitting. *Mater. Res. Bull.* **2019**, *116*, 98−105.
(50) Alom, M. S.; Ramezanipour, F. Electrocatalytic Activity of Layered Oxides $SrLaAl_{1/2}M_{1/2}O_4$ (M = Mn, Fe, Co) for Hydrogen- and Oxygen-Evolution Reactions. *Mater. Chem. Phys.* **2023**, *293*, No. 126942.
(51) Huang, X.; Zheng, H.; Lu, G.; Wang, P.; Xing, L.; Wang, J.; Wang, G. Enhanced Water Splitting Electrocatalysis over $MnCo_2O_4$

https://doi.org/10.1021/acsanm.3c00464
ACS Appl. Nano Mater. XXXX, XXX, XXX−XXX

via Introduction of Suitable Ce Content. *ACS Sustainable Chem. Eng.* **2019**, *7*, 1169−1177.
(52) Kananke-Gamage, C. C. W.; Ramezanipour, F. Variation of the Electrocatalytic Activity of Isostructural Oxides $Sr_2LaFeMnO_7$ and $Sr_2LaCoMnO_7$ for Hydrogen and Oxygen-Evolution Reactions. *Dalton Trans.* **2021**, *50*, 14196−14206.
(53) Shen, Y.; Chen, Y.; Fang, S.; Park, J. K.; Feng, K. Plasma-Modified Iron-Doped Ni_3S_2 Nanosheet Arrays as Efficient Electrocatalysts for Hydrogen Evolution Reaction. *Arabian J. Chem.* **2022**, *15*, No. 104317.
(54) Huang, L.; Lin, X.; Zhang, J.; Sheng, Z.; Wang, Q.; Zhang, F.; Qu, S.; Wang, Y. Facet Engineering of $NiCo_2S_4$ Electrocatalysts for Enhanced Hydrogen Evolution Reaction. *Appl. Catal., A* **2022**, *643*, No. 118803.
(55) Mohamed, I. M. A.; Kanagaraj, P.; Yasin, A. S.; Iqbal, W.; Liu, C. Electrochemical Impedance Investigation of Urea Oxidation in Alkaline Media Based on Electrospun Nanofibers towards the Technology of Direct-Urea Fuel Cells. *J. Alloys Compd.* **2020**, *816*, No. 152513.
(56) Palomar-Pardavé, M.; Romero-Romo, M.; Herrera-Hernández, H.; Abreu-Quijano, M. A.; Likhanova, N. V.; Uruchurtu, J.; Juárez-García, J. M. Influence of the Alkyl Chain Length of 2 Amino 5 Alkyl 1, 3, 4 Thiadiazole Compounds on the Corrosion Inhibition of Steel Immersed in Sulfuric Acid Solutions. *Corros. Sci.* **2012**, *54*, 231−243.
(57) Mohamed, M. J. S. High Bifunctional Electrocatalytic Activity of $FeWO_4/Fe_3O_4$@NrGO Nanocomposites towards Electrolyzer and Fuel Cell Technologies. *J. Electroanal. Chem.* **2021**, *897*, No. 115587.
(58) Mohamed, M. J. S.; Gondal, M. A.; Surrati, A. M. I.; Almessiere, M. A. Surface Oxygen Vacancy Defects Induced $CoTiO_{3-x}$ Perovskite Nanostructures for Highly Efficient Catalytic Activity from Acidic and Seawater Electrolysis. *Results Phys.* **2023**, *44*, No. 106179.

https://doi.org/10.1021/acsanm.3c00464
ACS Appl. Nano Mater. XXXX, XXX, XXX−XXX